A novel calibration system for heat flow meters: Experimental and numerical analysis

A NOVEL CALIBRATION SYSTEM FOR HEAT FLOW METERS: EXPERIMENTAL AND NUMERICAL ANALYSIS

Gino Cortellessa
Dipartimento di Ingegneria Civile e Meccanica, Università degli Studi di Cassino e del Lazio Meridionale, via G. Di Biasio 43, Cassino, Italy
g.cortellessa@unicas.it

Luigi Iacomini
Istituto Nazionale di Ricerca Metrologica (INRIM), Strada delle Cacce, 91 - 10135 Torino, Italy
l.iacomini@inrim.it

Corresponding author:
Dr. G. Cortellessa
Dipartimento di Ingegneria Civile e Meccanica, Università degli Studi di Cassino e del Lazio Meridionale,
Via G. Di Biasio 43, 03043 Cassino (FR), Italy
e-mail: g.cortellessa@unicas.it

Keywords:
Heat Flow Meter (HFM), CFD analysis, thermal transmittance, calibration system, uncertainty analysis.

ABSTRACT

The 2010/31/CE directive has pointed out the need to improve the buildings energy efficiency, since they are responsible for 40 % of energy consumption and 36 % of CO_2 emissions in the EU. The estimation and the reduction of thermal transmittance of building envelope components is crucial for the purpose.

Heat Flux Meters (HFMs), instruments devoted to this aim, unfortunately not always are provided with metrological traceability due to the lack of suitable reference standards, especially at critical conditions, such as in the low heat flux regime and low conductivity values.

In this paper, the authors propose a novel calibration standard for heat flux meters and discuss the metrological performance of this apparatus operating at critical conditions (low and moderate heat fluxes in the range 10 W/m^2 to 100 W/m^2). Besides experiments, a detailed numerical analysis has been conducted, validating obtained results against measurements. The developed standard can operate in two different modes: i) for thermal conductivity measurement and certification of reference materials; ii) for Heat Flux Meters (HFMs) calibration. A validated CFD model has then been employed to design, improve and analyze the calibration system in different operating conditions, also through a parametric analysis. Numerical results enabled us to improve and define the required heat flux uniformity in a specific sub-region of the measuring section. The experimental results supported the validation of the numerical model and a metrological characterization of the system which affords a combined standard uncertainty of better than 6% at low heat flows.

1. INTRODUCTION

In order to respect the constraints of the Kyoto Protocol on the reduction of greenhouse gas emissions in Europe, the 2002/91/CE directive has pointed out the substantial contribution of energy efficiency of buildings, since building heating/cooling systems are responsible for 40 % of energy consumption and 36 % of CO_2 emissions in the EU [1]. Such European directive, also adopted in Italy, set reference values for new buildings energy needs and building envelope components thermal transmittance. The duty of energy certification has also been introduced for new and existing buildings trading. As a consequence, from one side, research and development in insulation materials in the past 15 years increased exponentially [2] and, on the other side, it is even more necessary the field evaluation of the building envelope components thermal transmittance in order to: i) know the thermal transmittance of existing buildings in order to properly perform the energy certification; and ii) verify the declared envelope insulating performances for new buildings. When main design data about an existing building stratigraphy are not available, it can be necessary to perform invasive endoscopic tests to determine the stratigraphy and material typology. Alternatively, the thermal transmittance can be measured in situ, according to ISO 9869:2005 [3], by directly measuring the heat flux through building envelope components using an HFM. An HFM is basically made of a thin plate of known thermal conductivity, and by an integrated system for the measurement of the temperature difference across the plate itself. Time-consuming measurements and a proper data post-processing procedure are required to overtake not stationary conditions and to allow for the thermal conductance calculation.

The design, calibration and application method of HFM were standardized through the ASTM C1130:2017 [4], C177:2013 [5], ISO 8302:1991 [6], ASTM C 518:2017 [7], ISO 8301:1991 [8]. These standards describe two commonly used methods for the determination of the thermal conductivity: Guarded-hot plate (GHP) and Heat-flow meter methods. The thermal transmittance can be measured, according to ASTM C1046-95:2013 [9], ASTM C1363 [10], ASTM C1114 [11], EN12664 [12] standards using an HFM to perform the measurement of heat flux through a wall and using several temperature sensors to estimate the temperature gradient across the wall. By post-processing data, the thermal transmittance (or conductance) can be easily estimated. Thermal transmittance estimation is also important to obtain the so-called Certificate of excellence related to green building certification programs, such as LEED and ITACA [13]. The important aspects which needs to be investigated during a HFM calibration are: i) the dependence of the calibration curve on the temperature difference and on the average temperature referred to the wall under test; and ii) the dependence of the calibration curve on the thermal flux stability [14]. Therefore, the design of a suitable calibration apparatus for HFM must allow for an independent control of the thermal flux

crossing the HFM and the average temperature in the measurement section. In recent years, although many studies have been conducted on the metrological characteristics of such measuring instruments [15-17] and on calibration methods [18-20], the HFM used for measuring the energy performance of buildings were rarely calibrated, so the metrological traceability of the measurements is not always guaranteed. This happens because the measurement chain (made of a flow sensor, two or more temperature sensors and a data acquisition system) is quite complex and suitable standards are not always available at the National metrology institutes (NMIs) level to provide the first step in the traceability chain. As a result, different measurements performed by different devices are not comparable due to a lack of traceability in the measurement calibration chain.

Looking at the scientific literature, some authors designed Guarded Hot Plate (GHP) devices but mainly for the purpose of measurement the thermal conductivity. In particular, Dubois [21] presented a GHP apparatus designed for thermal conductivity measurement of high thickness crop-based specimens. High thickness samples, up to 40 cm, with an accuracy of 2% were analysed.

Reid [22] designed a GHP for high temperature applications. This apparatus was designed to measure thermal conductivity of soils at different moisture contents and for temperature ranging from -20°C to 200°C. An error around 2% was found for the thermal conductivity measurement.

Tleoubaev [23] developed a combined GHP and heat flow meter method for absolute thermal conductivity tests of moderate thermal conductivity materials (up to 10 W/mK). This combination of the two traditional steady-state methods provided significantly increased accuracy of the absolute thermal conductivity measurements of important materials such as ceramics, glasses, plastics, rocks, polymers, composites, fireproof materials, etc.

Reddy [24] designed a double-sided square guarded hot plate (SGHP) apparatus specifically for testing low to moderate thermal conductivity materials having thermal conductivities in the range of 0.02-3.0 $Wm^{-1}K^{-1}$. Le Quang [25] studied the size effect on the effective through-thickness conductivity of heterogeneous plates showing that the size effect of the effective through-thickness conductivity is more significant than the one of the effective in-plane conductivity. Cuce [26] presented a method based on thermal conductivity for material identification in scrap industry. The experimental thermal conductivity values of the samples were compared with the data available in the scientific literature and a good accordance was achieved.

Liu [27] performed numerical simulations with turbulence methods to study the effect of unsteady thermal boundary conditions on the temporal behaviour of heat transfer coefficient on a flat plate.

The calibration systems currently used have different limits related to: i) high and constant heat flux; ii) non-uniformity of the heat flux in the measurement section; iii) impossibility to control the heat flux at different temperatures.

In this paper the authors discuss the metrological performance of a prototype HFM reference standard operating at moderate heat fluxes. The prototype has been designed and realized in collaboration between the University of Cassino and Lazio Meridionale (UNICLAM) and the Istituto Nazionale di Ricerca Metrologica (INRIM). The proposed standard for HFM calibration relies on the GHP method. It was discussed in a previous work by one of the authors [28] who presented its design together with a preliminary CFD analysis in a heat flux range between 10 W/m^2 and 100 W/m^2. The design of the apparatus was flexible enough to be used for different applications, such as: i) the measurement of the thermal conductivity of insulating materials by generating a known heat flux and measuring the temperature difference across the thickness of the material under test; ii) the HFM calibration by an absolute method (i.e., by measuring the power generated by the main heater once the surface of the measuring section is known) or by a relative method (i.e., by measuring the temperature difference across a certified reference material with known thermal conductivity).

On the basis of the analysis results in [28], the authors developed a novel setup for the HFM prototype, with the objective of improving its potential applications and metrological performances. In particular, in this paper measurements carried out for average heat fluxes of about 10 W/m^2, 50 W/m^2 and 100 W/m^2 are presented and discussed. A comparison between the measurements obtained by absolute and relative methods has been performed to obtain a self-consistency proof and evaluating the uncertainty budget for each method. Besides, metrological performance of the proposed HFM reference standard has been numerically estimated by mean of a modern Computational Fluid Dynamic technique, exploiting the finite element based commercial code Comsol Multiphysics®. Numerical results have been validated against the experiments and the numerical model has then been applied to an extensive parameter analysis of the HFM prototype metrological performance.

2. EXPERIMENTAL APPARATUS

The proposed HFM standard prototype is shown in Figure 1, while a sketch of the prototype axi-symmetric cross-section is available in Figure 2, where a description of different components of the calibration system is reported.

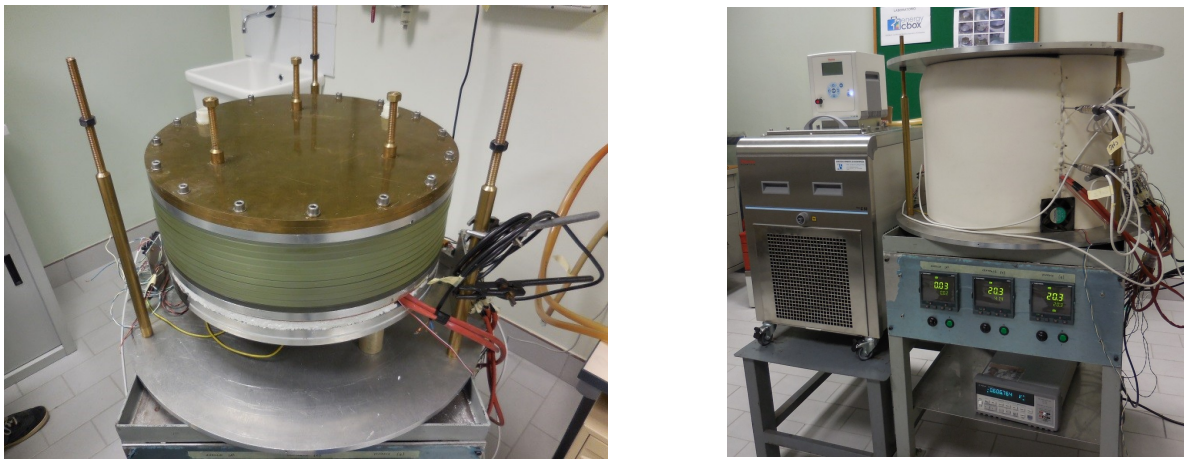

Figure 1. Prototype of the HFS standard assembled system.

The prototype is cylindrical and the bold dash-dot line represents its symmetry axis. In the above figure, the heaters are indicated in yellow, while the Pyrex® CRM samples no. 59, 60 and 73 are colored in green, blue and orange, respectively.

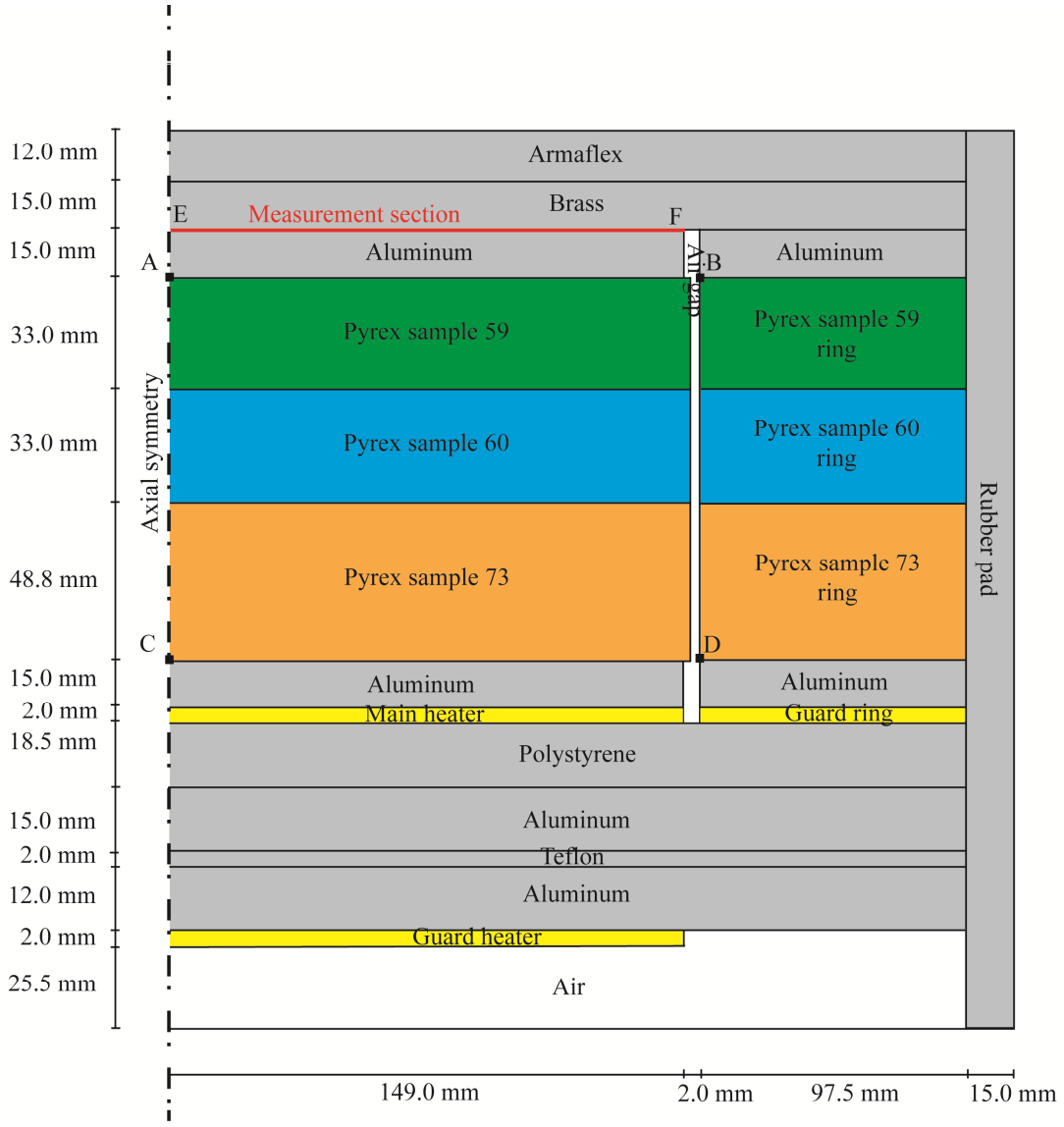

Figure 2 Prototype of the HFS standard: sketch of an axisymmetric section showing different components.

The calibration system is able to operate by absolute technique, by generating a known heat flux $\emptyset$ (W/m^2) in correspondence of the measurement section by means of three electric heaters: a main heater and two guard heaters. The electric power (W) supplied to the main heater is directly measured while the electric power supplied to the guard heaters is controlled by two proportional-integral-derivative (PID) controllers. The PID systems control the temperature difference across an air gap (between the main heater and the guard ring) and across the layers between the main heater and the lower guard heater to below 0.01 °C (see Figure 2). The temperature of the main heaters and the lower guard are measured by means of two Platinum Resistance Thermometers PRTs Pt-100, while the temperature difference between the main heater and the guard (ring heater) is measured by a thermopile made of eight type-J differential thermocouples with junctions evenly distributed on the annular interface between the heaters. In this way, the heat power (in W) supplied

to the main heater is directed toward the measurement section E-F, bold red line in the figure, where the Heat flux sensor (HFS) under calibration is positioned. The measurement section is a circular surface with a diameter of about 0.3 m. To minimize the distortion of heat flux lines, the HFS under calibration is matched to a complementary plate of similar material which covers the whole measurement surface, minimizing the air gap. Once the electric power to the main heater and the measurement section area are known, the heat flux across the HFS under calibration can be estimated. When operating in the absolute mode, the system is able to measure the thermal conductivity (in $\mathrm{Wm^{-1}K^{-1}}$) of a material, i.e. by generating a known heat flux and measuring the temperature difference across the material under test of known thickness [20, 29].

Three Pyrex® borosilicate glass plates with known thickness and known, certified, thermal conductivity are positioned as indicated in Figure 1, enabling the operation in the relative mode. The heat flux in the measuring section is now obtained by measuring the temperature drop across the Pyrex® glass plates. The glass samples are named, from bottom to top, sample no. 73 (with a thickness of 48.8 mm), no. 60 (with a thickness of 30.0 mm) and no. 59 (with a thickness of 30 mm), respectively. In correspondence to each glass sample, a concentric Pyrex® glass ring of the same thickness is installed, in order to minimize the radial heat dispersion from the main heater to the measuring section.

A brass plate sits on the top of the calibration system (as shown in Figure 1) to control the temperature in the calibration section by means of a temperature-controlled water flow supplied by thermostatic bath. Radial thermal dispersion to the surrounding environment was reduced by a double-layer insulating polymeric foam panels. Additional temperature sensors are placed in the points A, B, C and D in Figure 2 to further monitor the temperature distribution in the system.

3. UNCERTAINTY ANALYSIS

A measurement uncertainty analysis of the experiments, based on the ISO/IEC guideline on uncertainty estimation [30, 31], has been performed and presented in the following.

As described in Section 2, the experimental apparatus allows for heat flux meters to be calibrated by measuring alternatively: i) the electrical power in the measuring section (i.e. the absolute method); ii) the temperature drop across the reference glass layer (i.e. the relative method).

In the absolute method, when the electrical power is measured, the heat flux is estimated by the following equation:

$$\emptyset = \frac{P}{S} = \frac{V_H \cdot V_{Rs}}{S \cdot R_s} \tag{1}$$

where:

– $\emptyset$ is the measured heat flux, W m^{-2};
– P is the electric power, W;
– S is the area of the measuring cross-section, m^2;
– V_H, V_{Rs} are the voltage measured on the main heater and on the reference resistor, respectively, V;
– R_S is the electrical resistance of the reference resistor, ohm.

Neglecting the correlation between the estimated parameters, the combined standard uncertainty of measured heat flux is given by the following equation:

$$u_{\emptyset} = \sqrt{\left(\frac{V_{Rs}}{S \cdot R_s}\right)^2 u_{V_H}^2 + \left(\frac{V_H}{S \cdot R_s}\right)^2 u_{V_{Rs}}^2 + \left(\frac{V_H \cdot V_{Rs}}{S^2 \cdot R_s}\right)^2 u_S^2 + \left(\frac{V_H \cdot V_{Rs}}{S \cdot {R_s}^2}\right)^2 u_{R_s}^2} \quad (2)$$

where:

– $u_{\emptyset}$ is the standard uncertainty of the heat flux, W m^{-2};
– u_{V_H} and $u_{V_{Rs}}$ are the voltage standard uncertainties as measured on the main heater and on the reference resistor, respectively, V
– u_S is the standard uncertainty associated with the measuring cross-section, m^2;
– u_{R_s} is the standard uncertainty associated with the reference resistor, ohm.

On the other hand, when the temperature drop across the CRM glass layer is measured, the following equation is used:

$$\emptyset = \frac{\lambda_t \cdot \Delta T_{C-A}}{s_t} \quad (3)$$

where:

– λ_t is the Pyrex® glass thermal conductivity, in W m^{-1} K^{-1};
– ΔT_{C-A} is the temperature drop across the Pyrex® glass (temperature difference between points *C* and *A* in Figure 2), K;
– s_t is the thickness of a set of three glass layers (each of thickness s_i), m.

The combined standard uncertainty of the measured heat flux is obtained by the following equation:

$$u_{\emptyset} = \sqrt{\left(\frac{\Delta T_{C-A}}{s_t}\right)^2 u_{\lambda_t}^2 + \left(\frac{\lambda_t}{s_t}\right)^2 u_{\Delta T_{C-A}}^2 + \left(\frac{\lambda_t \cdot \Delta T_{C-A}}{s_t^2}\right)^2 u_{s_t}^2} \quad (4)$$

where:

– u_{λ_t} is the standard uncertainty of the Pyrex® thermal conductivity (from the reference material certificate), W m^{-1} K^{-1};
– $u_{\Delta T_{C-A}}$ is the standard uncertainty associated with the temperature drop across the glass layers, K;

– u_{s_t} is the standard uncertainty of the thickness of the set of three Pyrex layers, m.

The Pyrex® glass thermal conductivity has been determined by employing the equation for conduction in solid:

$$\lambda_t = \frac{s_t}{R_t} = \frac{\sum_{i=1}^{3} s_i}{\sum_{i=1}^{3} \left(\frac{s_i}{\lambda_i}\right)} \tag{5}$$

where $R_t = R_1 + R_2 + R_3$ (m^2 K W^{-1}) is the total thermal resistance to the heat flux given by three layers in series, each of thermal resistance $R_i = s_i/\lambda_i$. In this case, considering the correlation among the R_i estimations, u_{R_t} is calculated as follows:

$$u_{R_t} = \sqrt{u_{R_1}^2 + u_{R_1}^2 + u_{R_1}^2 + 2r\left(u_{R_1}u_{R_2} + u_{R_1}u_{R_3} + u_{R_2}u_{R_3}\right)} \tag{6}$$

The uncertainty associated with the conductivity u_{λ_t} was estimated by the following equation:

$$u_{\lambda_t} = \sqrt{\left(\frac{1}{R_t}\right)^2 u_{st}^2 + \left(\frac{s_t}{R_t^2}\right)^2 u_{R_t}^2} \tag{7}$$

The standard uncertainty of the temperature drop across the Pyrex® glass $u_{\Delta T_{C-A}}$ is:

$$u_{\Delta T_{C-A}} = \sqrt{2(u_t^2 + u_c^2) + u_{un}^2} \tag{8}$$

where:

– u_t is the calibration uncertainty of the temperature sensors, K;

– u_c is the uncertainty contribution due to the thermal contact, K;

– u_{un} is the uncertainty contribution due to the contact surface uniformity, K.

The standard uncertainty associated with the thickness of a set of three glass layers, u_{s_t}, was estimated through the corresponding uncertainties of each *i-th* pyrex layer u_{s_i}, in turns estimated with the following equation:

$$u_{s_i} = \sqrt{u_l^2 + \frac{RES^2}{12} + \left(\frac{\sigma_i}{\sqrt{N_i}}\right)^2} \tag{9}$$

$$u_{s_t} = \sqrt{u_{s_1}^2 + u_{s_2}^2 + u_{s_3}^2 + 2r\left(u_{s_1}u_{s_2} + u_{s_1}u_{s_3} + u_{s_2}u_{s_3}\right)} \tag{10}$$

where:

– u_l is the calibration standard uncertainty of the gauge instrument, m;

– RES is the resolution of the gauge instrument, m;

– $\sigma/\sqrt{N}$ is a type-A uncertainty [32, 33] associated with the standard deviation σ of N measurements, mm.

– r is the correlation coefficient assumed equal to 0.5, since measurements of single layer thickness have been performed with the same instrument.

In Table 1 and Figure 3 the estimated expanded uncertainties for the developed calibration apparatus are summarized.

Table 1. Expanded uncertainty of the calibration apparatus

Ø Nominal heat flux, Wm^{-2}	*$U_{Ø}$, Expanded uncertainty for the absolute method, %*	*$U_{Ø}$, Expanded uncertainty for the relative method, %*
10	1.8	5.7
50	1.5	3.2
100	1.5	2.8

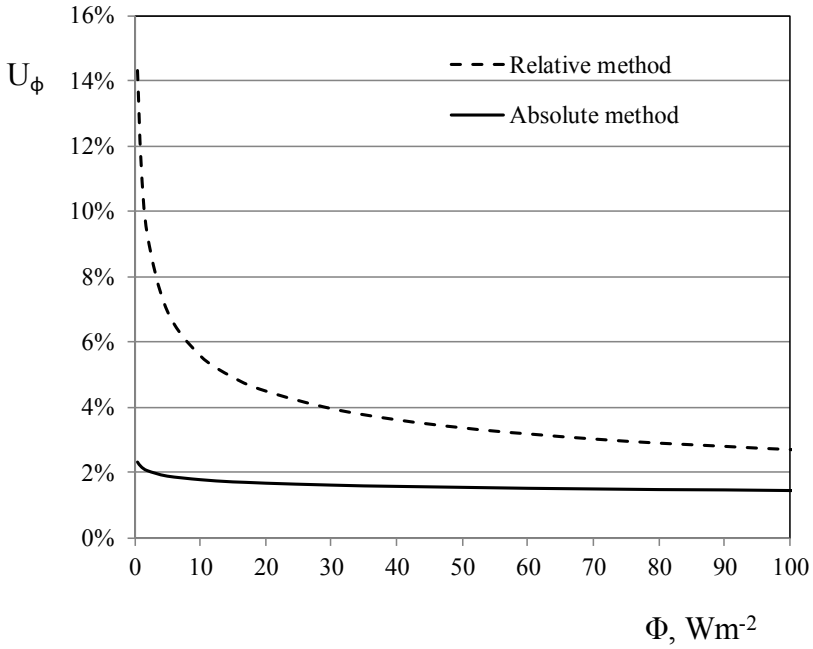

Figure 3. Expanded uncertainty trend as a function of the heat flux

4. MATHEMATICAL MODEL, COMPUTATIONAL DOMAIN AND BOUNDARY CONDITIONS

Temperature distribution inside the proposed HFM standard prototype has been numerically reproduced through modern Computational Fluid Dynamic (CFD) technique Simulations employing the finite element based commercial software Comsol Multiphysics®.

Since the HFM calibration system described in section 2 has a cylindrical shape, the experimental apparatus has been numerically reproduced by means of axial symmetric steady-state simulations.

The experimental apparatus has been reproduced by a two-dimensional axial symmetric computational domain, that is available in Figure 4 together to the boundary conditions employed and a detail of the computational grid, composed by 80045 triangular elements and chosen on the basis of a mesh sensitivity analysis.

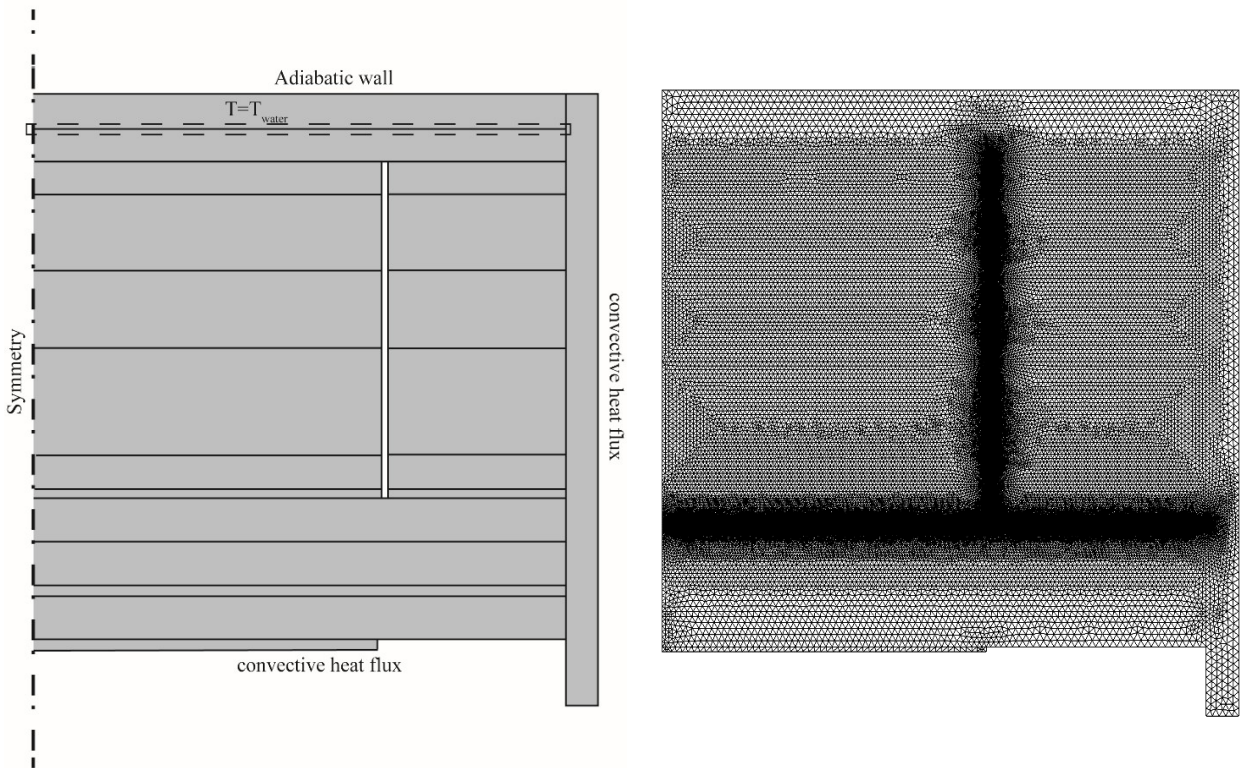

(a) (b)

Figure 4. Numerical simulation of the HFM standard prototype: computational domain and boundary condition employed (left) and a detail of the computational grid composed by 80045 triangular elements (right).

An appropriate set of boundary conditions (BCs) has been imposed and indicated within the computational domain (Figure 4a). In particular, a constant and uniform temperature (T_{water}) was imposed between the insulating foam panels and the brass plates to reproduce the thermal effect of the thermostatic bath. Additionally, a convective heat flux was evaluated and applied on the right vertical wall and the lower surface of the computational domain, while an adiabatic boundary condition was applied to the upper horizontal surface.

In order to take into account conductive heat transfer within the computational domain, temperature field in correspondence of the equipment has been numerically reproduced by solving the well-known energy conservation equations [34-37]. Partial differential equations (PDEs) constituting the employed mathematical model are available in the scientific literature and are not reported here for brevity.

A thermal heat source is numerically imposed in correspondence of the main heater in order to obtain the desired heat flux at the measuring section. The calculation procedure is based on an iterative process, that allows the numerical determination of the heat power to be imposed in correspondence of the guard heaters. In particular, the following calculation steps are followed: i) impose a heat power on the main heater; ii) perform first simulation with zero heat power imposed in correspondence of the two guard heaters; ii) calculate the temperature difference across the mean heater and the lower guard heater in axial direction and between the main heater and the side guard heater in the radial direction; iii) if temperature differences are larger than 0.01°C then increase/decrease heat power of the two guards and repeat simulation until convergence.

5. MODEL VALIDATION

Results from numerical investigations have been firstly validated by comparison against the data collected during experiments. Based on available measurements, the main input parameters for numerical simulation are reported in Table 2.

Table 2. Main input parameters used in the numerical investigations.

Parameter	Value
Ambient temperature, T_a	23.0 °C
Ambient pressure, p_a	101325 Pa
Water temperature, T_{water}	29.75 °C - 32.80 °C
Main heater power, E_p	7.07 W - 3.53 W - 0.71 W
Pyrex conductivity, $\lambda_{pyrex}(T)$	$1.1036+1.659\text{x}10^{-3}T-3.982\text{x}10^{-6}T^2+6.764\text{x}10^{-9}T^3$ W/m/K
Pyrex density, ρ_{pyrex}	2230 kg/m^3
Pyrex specific heat, $c_{p,pyrex}$	837 J/kg/K
Aluminum conductivity, $\lambda_{aluminum}$	120 W/m/K
Aluminum density, $\rho_{aluminum}$	2702 kg/m^3
Aluminum specific heat, $c_{p,aluminum}$	896 J/kg/K
Rubber pad conductivity, λ_{rubber}	0.073 W/m/K
Rubber pad density, ρ_{rubber}	1000 kg/m^3
Rubber pad specific heat, $c_{p,rubber}$	1000 J/kg/K
Teflon conductivity, λ_{teflon}	0.23 W/m/K
Teflon density, ρ_{teflon}	2140 kg/m^3
Teflon specific heat, $c_{p,teflon}$	1000 J/kg/K
Polystyrene, conductivity, $\lambda_{polystyrene}$	0.054 W/m/K
Polystyrene, density, $\rho_{polystyrene}$	15 kg/m^3
Polystyrene specific heat, $c_{p,polystyrene}$	1220 J/kg/K
Armaflex, conductivity, $\lambda_{polystyrene}$	0.038 W/m/K
Armaflex, density, $\rho_{polystyrene}$	70 kg/m^3
Armaflex specific heat, $c_{p,polystyrene}$	1000 J/kg/K

Simulations were performed for three different values of the main heater power in order to generate an estimated heat flux of 10 W/m^2, 50 W/m^2 and 100 W/m^2, from the main heater towards the

measuring section. The temperature contour in both solid and fluid region, as obtained for a heat flux equal to 100 W/m^2 and a thermostatic bath temperature of 32.80 °C is shown in Figure 5a.

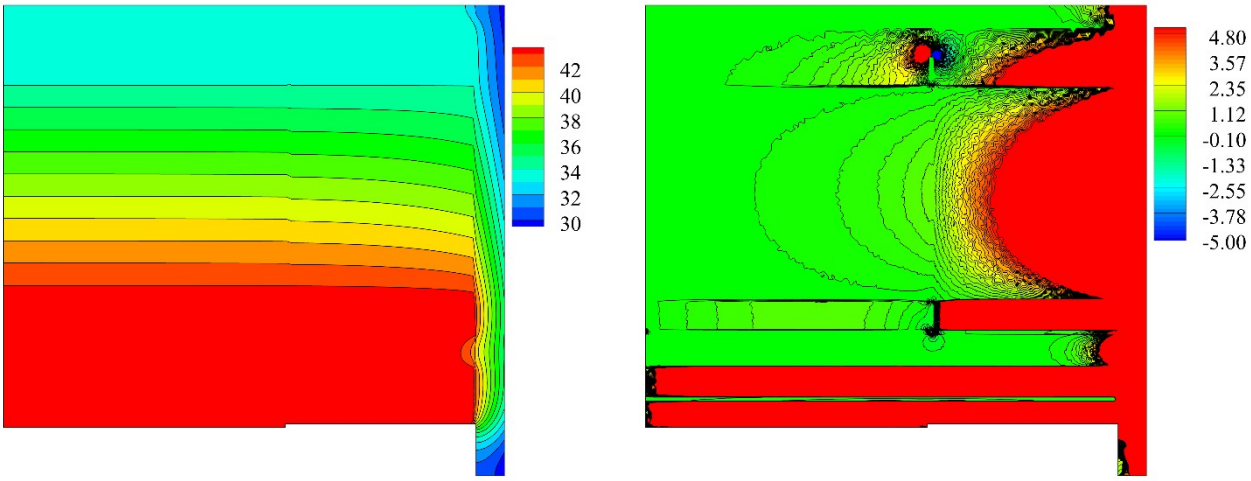

Figure 5. Temperature contour (a) and radial heat flux limited between -5 W/m^2 and 5 W/m^2 (b) obtained for a generated heat flux on the mean heater equal to 100 W/m^2.

The maximum temperature is reached in proximity of the main heater (44.08 °C) while the surrounding environment presents the lowest temperature (23 °C).

Figure 5b represents the heat flux contour along the radial direction, in the 5 W/m^2 to -5 W/m^2 span. Small radial heat flux dispersions are visible in the measurement section (lower than 1 W/m^2). The green zones clearly indicate that the heat flux radial dispersions are fairly limited thanks to the effective operation of the lower and radial thermal guards.

Comparisons between experiments and numerical results for the investigated heat fluxes are available in Table 3 for heat fluxes of 100 W/m^2, 50 W/m^2 and 10 W/m^2, respectively. Eight experiments, obtained for different liquid bath temperatures, ranging between 29.75 °C and 32.80 °C, were selected for the purpose of validating the numerical model. All the tests were carried out with a surrounding environment temperature equal to 23 °C.

In order to obtain a heat flux of 100 W/m^2 from the main heater towards the measurement section, a heat-source power of 7.07 W was numerically imposed in the heater domain and later measured by the electric power delivered to the main heater. Similarly, source power terms in the simulation and measured electric powers are 3.53 W for a heat flux of 50 W/m^2, and 0.71 W for a heat flux of 10 W/m^2.

Table 3. Comparison between the experiments and numerical results obtained in correspondence of three different heat flux, generated by the main heater, equal to 10, 50 and 100 W/m^2.

Test number	**1**	**2**	**3**	**4**	**5**	**6**	**7**	**8**
Heat flux at the main heater (W/m^2)	100	50	50	50	10	10	10	10
Thermostatic bath temperature (°C)	32.80	30.76	31.55	30.07	29.75	29.76	30.88	31.87
Heat power at the main heater (W)	7.07	3.53	3.53	3.53	0.71	0.71	0.71	0.71
Experimental temperature of point A (°C)	33.95	32.26	32.34	30.90	30.06	30.07	31.07	32.05
Numerical temperature of point A (°C)	33.98	32.27	32.35	30.91	30.06	30.07	31.07	32.05
Experimental temperature of point B (°C)	33.90	31.60	32.14	30.72	29.80	29.81	30.89	31.84
Numerical temperature of point B (°C)	33.97	32.27	32.35	30.91	30.06	30.07	31.07	32.05
Experimental temperature of point C (°C)	43.79	37.15	37.26	35.91	31.00	31.02	31.98	32.91
Numerical temperature of point C (°C)	43.73	37.16	37.24	35.82	31.02	31.03	32.02	32.99
Experimental temperature of point D (°C)	43.76	37.13	37.23	35.88	31.00	31.02	32.00	32.93
Numerical temperature of point D (°C)	43.75	37.17	37.25	35.83	31.02	31.03	32.03	33.00
Experim. ΔT between point C and point A (°C)	9.84	4.89	4.92	5.01	0.94	0.95	0.91	0.86
Numerical ΔT between point C and point A (°C)	9.76	4.89	4.89	4.91	0.95	0.96	0.95	0.94
Heat power at the radial guard heater (W)	16.17	8.59	8.44	8.21	2.71	2.72	2.88	3.11
Heat power at the lower guard heater (W)	7.39	4.45	4.19	3.80	2.51	2.51	2.79	3.18
Experimental heat flux (relative method) (W/m^2)	99.67	49.26	49.60	50.42	9.43	9.49	9.14	8.67
Numerical average heat flux on the pyrex (W/m^2)	98.75	49.21	49.25	49.33	9.56	9.56	9.51	9.44
Numerical heat flux in section E-F (W/m^2)	98.52	49.06	49.11	49.20	9.47	9.47	9.41	9.32

In the case of a nominal heat of flux 100 W/m^2, the average heat flux across the three Pyrex® layers, estimated with the relative method was equal to 99.67 W/m^2. Similarly, when a heat flux of 50 W/m^2 leaves the main heater towards the direction of the measurement section, the heat flux estimated with the relative method ranges between 49.26 W/m^2 and 50.22 W/m^2. Finally, in the case of a heat flux of 10 W/m^2 the estimates were between 9.32 W/m^2 and 9.47 W/m^2.

Comparing the heat flux values as measured by the relative method with the numerical results, a difference of 0.23 % is observed for a heat flux of 100 W/m^2 (test number 1). When a heat flux of 50 W/m^2 is applied, the minimum heat flux difference obtained is equal to 0.26 % while maximum heat flux difference is equal to 0.30 % (test number 2, 3 and 4). Finally adopting a heat flux of 10 W/m^2, the minimum heat flux difference obtained is equal to 0.94 % while maximum heat flux difference is equal to 1.27 % (test number 5, 6, 7 and 8).

The measurement uncertainty associated with the measured heat flux with the relative method ranges between 5.7%, when the heat flux is equal to 10 W/m^2, and 2.8%, when the heat flux is 100 W/m^2. As shown, experiments and numerical results are compatible and the proposed numerical model is validated.

In Figure 6, the deviations between the experimental and numerical heat fluxes and the heat fluxes imposed at the main heater are reported as a function of the liquid bath temperature for all tests.

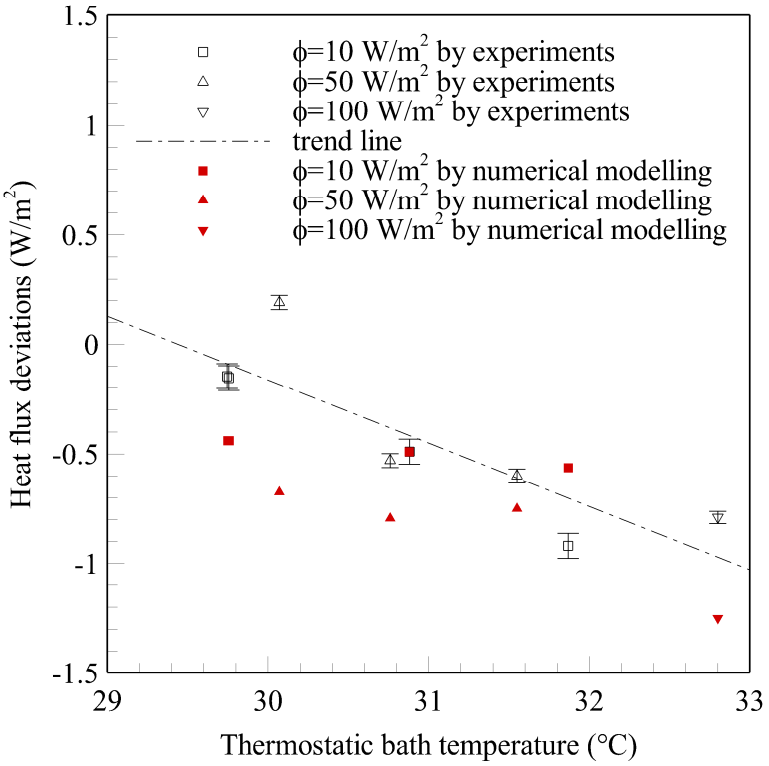

Figure 6. Numerical and experimental heat flux deviations as a function of the thermostatic bath temperature.

From this figure, a good agreement was found between the numerical and experimental data. In particular, it is evident that for lower liquid bath temperatures, lower heat flux deviations are obtained.

In Table 3, the results are also shown in terms of temperature in the selected points A, B, C and D (see Figure 2) and temperature difference between points A and C (to estimate the axial temperature variation among the glass plates). All the measurement uncertainties associated with experiments are also reported in the table.

In the case of 100 W/m^2, a maximum temperature deviation of 0.06°C between experiments and numerical results was observed in all points of the computational domain, while the deviation in the temperature between points C and A is equal to 0.08°C.

In the case of 50 W/m^2, the maximum experimental-to-numerical temperature deviation was equal to about 0.67°C, while in the case of 10 W/m^2, it amounted to 0.26°C. As regards the temperature difference between points C and A, the experiment-to-simulation temperature deviation was below 0.08 °C for both 50 W/m^2 and 10 W/m^2 heat fluxes.

6. PARAMETRIC ANALYSIS

In this section, the effects on the heat flux uniformity in the measurement section E-F of the calibration system due to the variation of same geometrical and thermo-fluid-dynamic parameters are analyzed. In particular, considering as reference case the configuration described in Section 4, the following influence factors have been taken into account: external air temperature; thickness of the rubber pad; diameter of aluminum plate over the Pyrex® glass sample no. 59; glass samples diameter; thickness of air gap between the glass samples and rings.

External air temperature

Experiments on the calibration system were carried out by keeping the temperature in the laboratory at 23 ± 0.01 °C. On the other hand, the variation of the heat flux value in the measuring section and its uniformity, related to changes in the external air temperature has been numerically investigated and the results are discussed in this paragraph. In particular, the environmental air temperature was varied between 5°C and 30°C. The results are depicted in Figure 7, where Figure 7(a) shows the heat flux in the measuring section and the non-uniformity as a function of the radius in the range $0\ \text{m} \leq r \leq 0.025\ \text{m}$, for three different air temperatures: 5 °C, 15 °C and 30 °C.

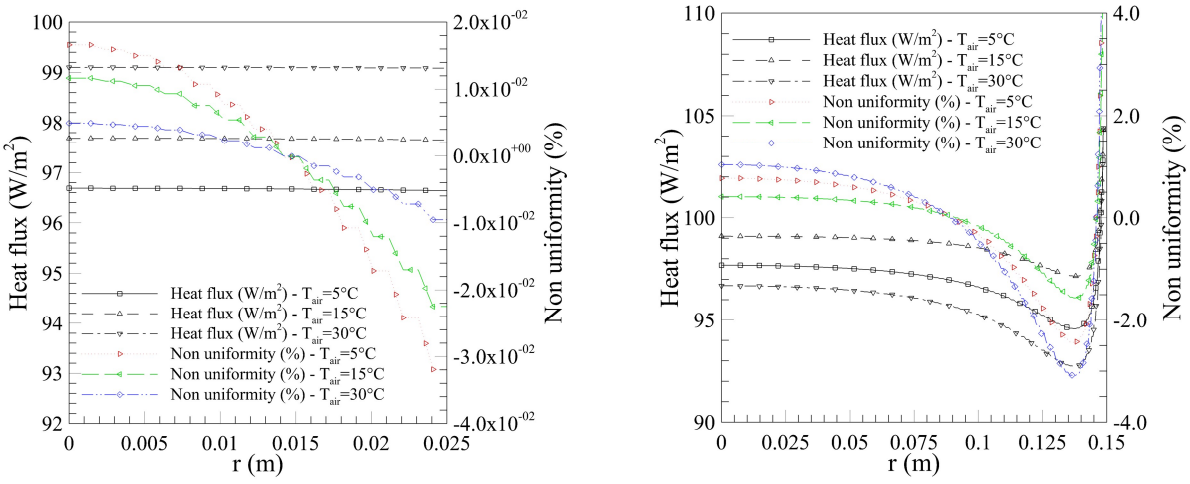

Figure 7. Heat flux profile for different air temperature as a function of the radius covering portion of the ring necessary for the HFS calibration (a) and as a function of the radius covering the full measurement section E-F (b).

The above range is justified by the need of calibrating small circular HFS. The heat flux distribution and its non-uniformity in the entire aluminium plate, in correspondence of the measuring section E-F, is shown in Figure 7(b). From the analysis of the results, it is possible to observe that the heat flux is very uniform in the radius range $0\ \text{m} \leq r \leq 0.025\ \text{m}$, with a decrease correlated to the

external air temperature. In the whole radius range, the maximum non-uniformity is equal to about 0.03 %. In the air temperature range considered, the heat flux variation is equal to 2.4 W/m^2.

Thickness of the rubber pad

The thickness of the rubber pad, used as insulation to minimize heat losses in the calibration system, is equal to 15 mm. Additional numerical simulations were performed in order to investigate the effect of its thickness variation on the heat flux and its uniformity in the measurement section. The thickness range was 0 mm to 30 mm. Figure 8 shows the heat flux and its uniformity as a function of the radius for different thickness of the rubber pad: 0 mm, 7.5 mm, 15 mm and 30 mm.

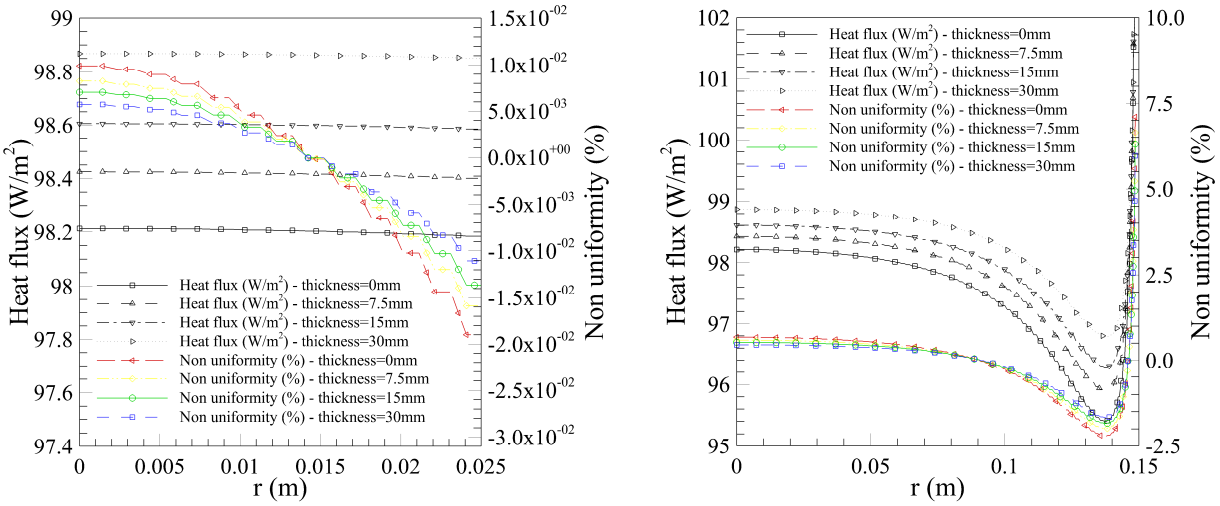

Figure 8. Heat flux profile for different thickness of insulant as a function of the radius covering portion of the ring necessary for the HFS calibration (a) and as a function of the radius covering the full measurement section E-F (b).

Similarly to the previous case, in Figure 8(a) only the radius range $0\ \text{m} \leq r \leq 0.025\ \text{m}$ has been considered, while in Figure 8(b) the radius range in the entire E-F section is considered. From the results, it is possibile to observe the heat flux is an increasing function of the rubber pad thickness and its maximum value was obtained in correspondence of a 30-mm tickness. Also in this case, the heat flux is very uniform in the radius range $0\ \text{m} \leq r \leq 0.025\ \text{m}$. On the other hand, by considering, the full measurement section E-F the maximum heat flux non-uniformity was slightly larger than 10 %.

Diameter of aluminum over the Pyrex® sample no. 59

Further numerical investigations were performed by varying the diameter of aluminum disc over the Pyrex sample no. 59 within its tolerance band (from 296.74 mm and 300.74 mm). Figure 9 shows the heat flux and its uniformity as a function of the radius for minimun, mean and maximum

aluminium disc diameter value. Similarly to the previous case, in Figure 9(a) only the radius range $0\ \text{m} \leq r \leq 0.025\ \text{m}$ has been considered, while in Figure 9(b) the entire E-F section range is reported. From the analysis of the results, it is possible to observe that increasing the aluminum diameter the heat flux is subject to a small reduction of about 0.077 % when the radius ranges between 0 m and 0.025 m. In addition, the heat flux is very uniform in such radius range but, considering the radius covering the entire measurement section E-F, the heat flux non-uniformity was larger than 20 %.

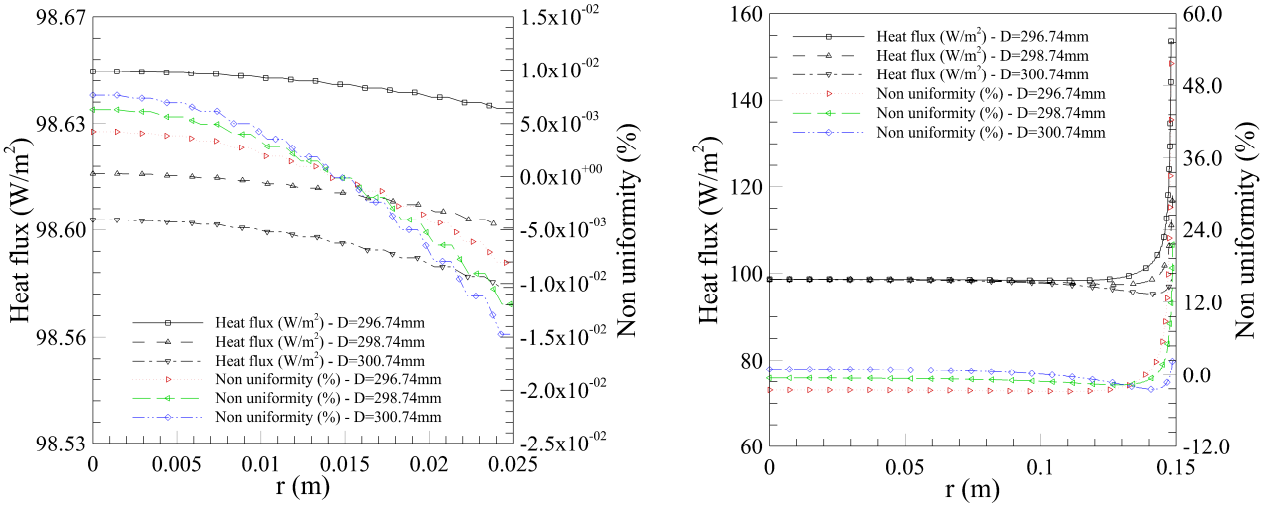

Figure 9. Heat flux profile for different aluminium diameters as a function of the radius covering portion of the ring necessary for the HFS calibration (a) and as a function of the radius covering the full measurement section E-F (b).

Pyrex® glass diameter

In this paragraph, the system performance dependence on the reference glass plates diameter was numerically investigated. In the simulations, the diameters of the three plates were varied within their tolerance band. The results are shown in Figure 10, Figure 11 and Figure 12 in the radius range between 0 mm and 0.025 m and in the entire measuring section E-F, in the same way as discussed in previous sub-sections. With reference to radius range from 0 m to 0.025 m, from the analysis of these figures it is possible to observe that: by increasing the Pyrex no.59 diameter within its tolerance band, a heat flux reduction of 0.20 % was obtained (Figure 10); by increasing the Pyrex® no. 60 diameter within its tolerance band, a heat flux increase of 0.70 % was obtained (Figure 11); and, finally, by increasing the Pyrex® no. 73 diameter within its tolerance band, a heat flux reduction of 0.79 % was obtained (Figure 12). The heat flux presents an excellent uniformity in the range from 0 m to 0.025 m, while the temperature non-uniformity significantly increases for radiuses larger than 0.1 m.

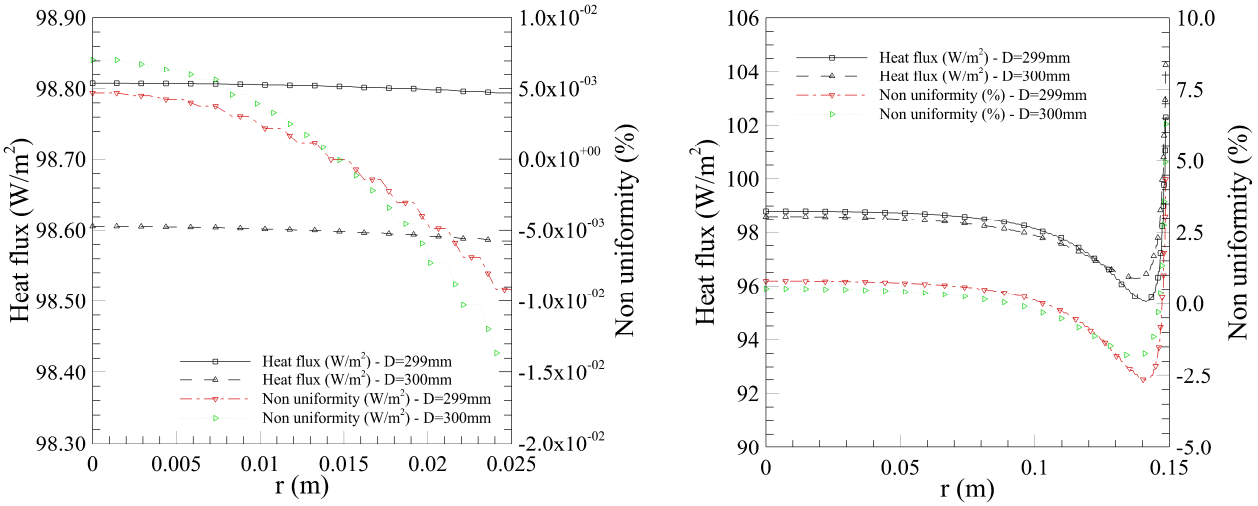

(a) (b)

Figure 10. Heat flux profile for different pyrex59 diameters as a function of the radius covering portion of the ring necessary for the HFS calibration (a) and as a function of the radius covering the full measurement section E-F (b).

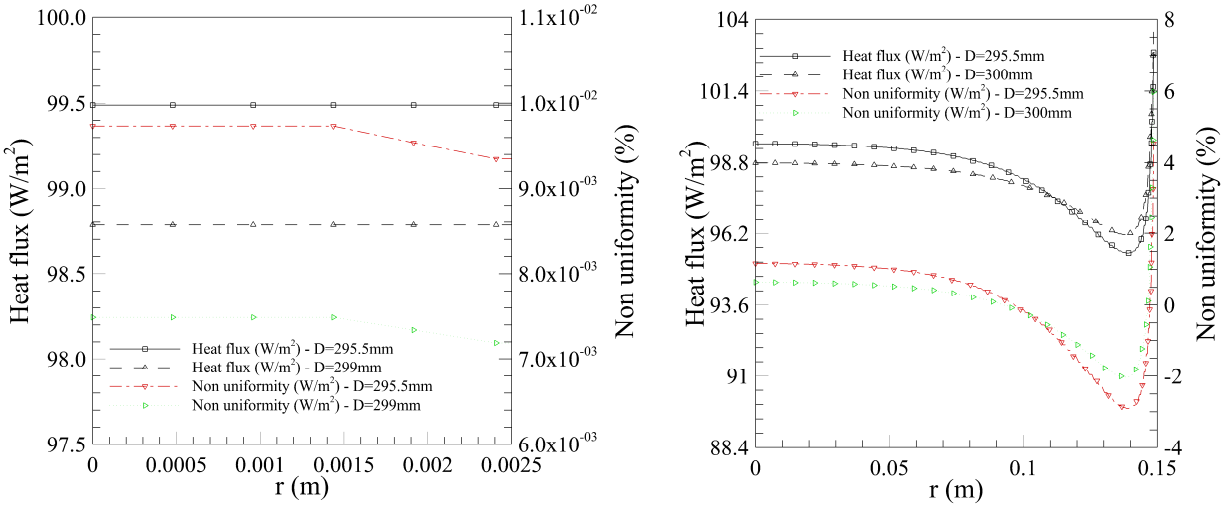

(a) (b)

Figure 11. Heat flux profile for different pyrex60 diameters as a function of the radius covering portion of the ring necessary for the HFS calibration (a) and as a function of the radius covering the full measurement section E-F (b).

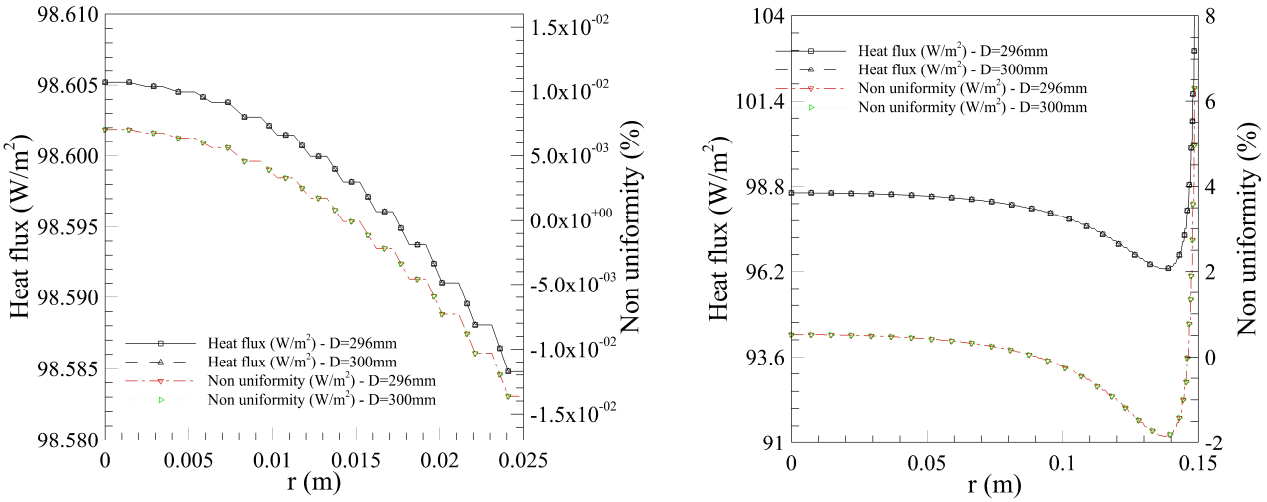

Figure 12. Heat flux profile for different pyrex73 diameters as a function of the radius covering portion of the ring necessary for the HFS calibration (a) and as a function of the radius covering the full measurement section E-F (b).

Thickness of the air gap between the Pyrex® samples and the rings

Finally, the calibration system performance variation as a function of the air gap thickness between the Pyrex® samples and the Pyrex® ring (equal to 8mm) was numerically investigated (Figure 13). Nevertheless, referring to the radius range from 0 m to 0.025 m, no significant variations in the heat flux and its uniformity were found. In particular, heat flux variation was not larger than 0.020 % and maximum non-uniformity was not larger than 0.001 %.

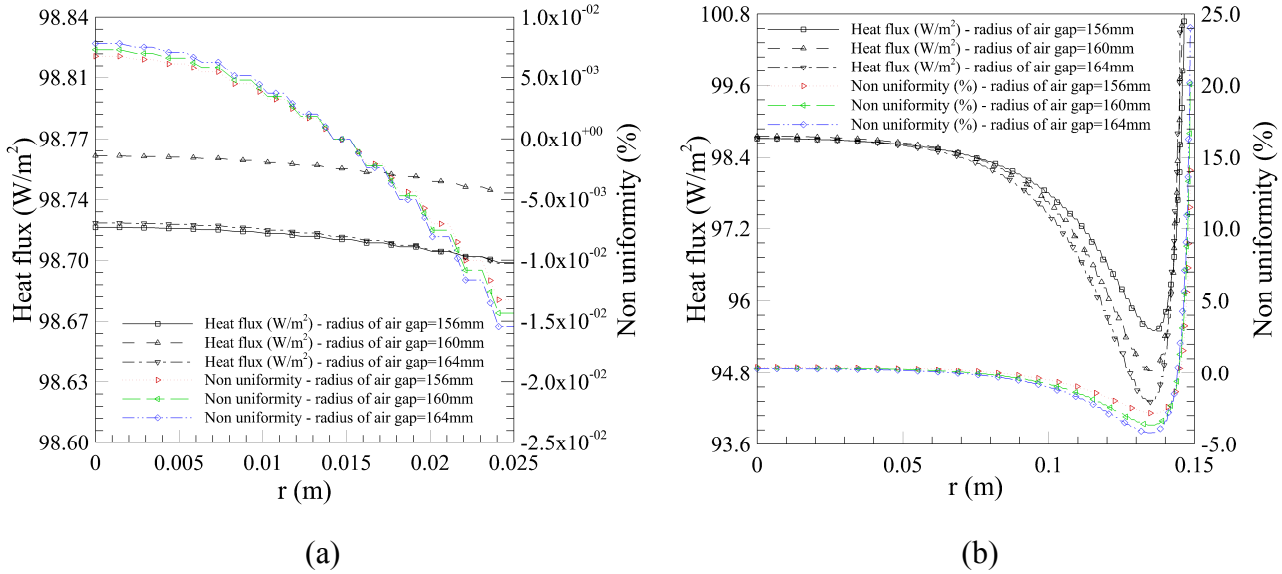

Figure 13. Heat flux profile for different thickness of air gap as a function of the radius covering portion of the ring necessary for the HFS calibration (a) and as a function of the radius covering the full measurement section E-F (b).

7. CONCLUSIONS

In the present paper, the authors propose an innovative HFS calibration system, developed in collaboration between UNICLAM and INRIM. The metrological performances of the proposed standard system have been investigated, both experimentally and numerically. The system can be used in two different modes: i) measurement of the materials thermal conductivity by the generation of a known thermal flow; ii) calibration of a HFS by an absolute method (measurement of the energy supplied by the heater and the cross-section area covered by the thermal flow) or by a relative method (measurement of the temperature difference of a material specimen with known conductivity and thickness). In order to ensure the required heat flux uniformity, the guarded hot plate approach has been adopted, and the system can be applied to HFS calibration in the range from approximately 10 W/m^2 to 100 W/m^2. An experimental campaign was carried out encompassing the generated heat fluxes of 10 W/m^2, 50 W/m^2 and 100 W/m^2. A comparison between the measurements obtained by absolute and relative methods was performed and a detailed uncertainty analysis of the generated heat flux was carried out. The combined standard uncertainty affecting the measured heat flux according to the relative method ranges between 5.7 %, at the lowest heat flux, and 2.8 % when the heat flux is near 100 W/m^2.

In order to further improve the calibration system performance, the temperature distribution has been modeled by employing modern Computational Fluid Dynamic (CFD) techniques. The numerical results were initially validated against the experiments and a good agreement was found. Once validated, the numerical tool has been applied to investigate the heat flux uniformity in the measurement section E-F as a function of the variation of the following geometrical and thermo-fluid-dynamic parameters: external air temperature; thickness of the rubber pad; aluminum plate diameter over the Pyrex® glass sample no. 59; Pyrex® samples diameter; thickness of air gap between the Pyrex® glass samples and the rings. It has been observed that the required heat flux uniformity is obtained in a sub-region of the measuring section E-F, prompting that the proposed standard calibration system can be used for the calibration of small-sized HFS.

8. REFERENCES

[1] https://ec.europa.eu/energy/en/topics/energy-efficiency/buildings, in: Commission E. (Ed.), 2018.

[2] S. Jinhua J.L., Thermal Analysis and Flame Spread Behavior of Building-Used Thermal Insulation Materials, in: Fire Science and Technology, Tsukyba, Japan, 2016, pp. 45-59.

[3] ISO 9869-1:2014, Thermal insulation - Building elements - In-situ measurement of thermal resistance and thermal transmittance - Part 1: Heat flow meter method, in, ISO, 2014.

[4] ASTM C1130: Standard Practice for Calibration of Thin Heat Flux Transducers, in, ASTM INTERNATIONAL, 2017.

[5] ASTM C177-13: Standard Test Method for Steady-State Heat Flux Measurements and Thermal Transmission Properties by Means of the Guarded-Hot-Plate Apparatus, in, ASTM International, 2013.
[6] ISO 8302: Thermal insulation - Determination of steady-state thermal resistance and related properties - Guarded hot plate apparatus, in, ISO, 1991.
[7] ASTM C518-17: Standard Test Method for Steady-State Thermal Transmission Properties by Means of the Heat Flow Meter Apparatus, in, ASTM International, 2017.
[8] ISO 8301: Thermal insulation - Determination of steady-state thermal resistance and related properties - Heat flow meter apparatus, in, ISO, 1991.
[9] ASTM C1046-95: Standard Practice for In-Situ Measurement of Heat Flux and Temperature on Building Envelope Components, in, ASTM International, 2013.
[10] ASTM C1363: Standard Test Method for Thermal Performance of Building Materials and Envelope Assemblies by Means of a Hot Box Apparatus, in, ASTM INTERNATIONAL, 2011.
[11] ASTM C1114- 06: Standard Test Method for Steady-State Thermal Transmission Properties by Means of the Thin-Heater Apparatus, in, ASTM INTERNATIONAL, 2013.
[12] CSN EN 12664 - Thermal performance of building materials and products - Determination of thermal resistance by means of guarded hot plate and heat flow meter methods - Dry and moist products of medium and low thermal resistance, in, European Standards, 2001.
[13] Cole R.J., Jose Valdebenito M., The importation of building environmental certification systems: international usages of BREEAM and LEED, Building Research & Information, 41 (2013) 662-676.
[14] Guattari C., Evangelisti L., Gori P., Asdrubali F., Influence of internal heat sources on thermal resistance evaluation through the heat flow meter method, Energy and Buildings, 135 (2017) 187-200.
[15] Van der Graaf F., Heat flux sensors, in: W.Gopel (Ed.) Sensors, New York, 1989, pp. 295-322.
[16] Flanders S.N., Heat flux trasducers measure in-situ building thermal performance, Journal of Thermal Insulation and Building Environments, 18 (1994) 28-52.
[17] Hauser R.L., Construction and performance of in situ heat flux trasducers, in: Bales (Ed.) Building Applications of Heat Flux Trasducers - ASTM STP 885, 1985, pp. 172-183.
[18] Murthy V., Tsai B., Saunders R., Facility for calibrating heat flux sensors at NIST: an overview, in: M.E.Ulucakli (Ed.) ASME Heat Transfer Division, New York, 1997, pp. 159-164.
[19] Lackey J., Normandin N., Marchand R., Kumaran K., Calibration of Heat Flow Meter Apparatus, J. Thermal Insul. and Bldg. Envs., 18 (1994) 128-144.
[20] Bomberg M., Solvason K.R., Comments on Calibration and Design of Heat Flow Meter, Thermal Insulation, Materials and Systems fo Energy Conservation in the '80s - ASTM STP 789, (1983) 277-292.
[21] Dubois S., Lebeau F., Design, Construction and Validation of a Guarded Hot Plate Apparatus for Thermal Conductivity Measurement of High Thickness Crop-Based Specimens, Materials and structures, 48 (2013) 407-421.
[22] Reid D., Guarded hot plate apparatus design and construction for thermal conductivity measurements, in, Ryerson University, Toronto, Ontario, Canada, 2005.
[23] Tleoubaev A., Brzezinski A., Combined Guarded-Hot-Plate and Heat Flow Meter Method for Absolute Thermal Conductivity Tests Excluding Thermal Contact Resistance, in: Thermal Conductivity 27/Thermal Expansion 15, Knoxville, Tennessee, USA, 2003.
[24] Reddy K.S., Jayachandran S., Investigations on design and construction of a square guarded hot plate (SGHP) apparatus for thermal conductivity measurement of insulation materials, Int. J. Therm. Sci., 120 (2017) 136-147.
[25] Le Quang H., Pham D.C., Bonnet G., Size effect in through-thickness conductivity of heterogeneous plates, Int. J. Therm. Sci., 79 (2014) 40-50.
[26] Cuce E., Cuce P.M., Guclu T., Besir A., Gokce E., Serencam U., Serencam H., A novel method based on thermal conductivity for material identification in scrap industry: An experimental

validation, Measurement: Journal of the International Measurement Confederation, 127 (2018) 379-389.
[27] Liu C.L., Gao C., von Wolfersdorf J., Zhai Y.N., Numerical study on the temporal variations and physics of heat transfer coefficient on a flat plate with unsteady thermal boundary conditions, Int. J. Therm. Sci., 113 (2017) 20-37.
[28] Arpino F., Dell'Isola M., Ficco G., Iacomini L., Fernicola V., Design of a calibration system for heat flux meters, International Journal of Thermophysics, 32 (2011) 2727-2734.
[29] Bomberg M., Solvason K.R., Discussion of Heat Flow Meter Apparatus and Transfer Standards Used for Error Analysis, in: Guarded Hot Plate and Heat Flow Meter Methodology - ASTM STP 879, 1985, pp. 140-153.
[30] UNI CEI 70098-3: Incertezza di misura - Parte 3: Guida all'espressione dell'incertezza di misura, in, UNI, 2016.
[31] BIPM, Evaluation of measurement data - The role of measurement uncertainty in conformity assessment, in: GUM: Guide to the Expression of Uncertainty in Measurement, 2012.
[32] Coleman H.W., Steele W.G., Experimentation and Uncertainty Analysis for Engineers, 2 ed., USA, 1999.
[33] Betta G., Dell'Isola M., Frattolillo A., Experimental design techniques for optimising measurement chain calibration, Measurement: Journal of the International Measurement Confederation, 30 (2001) 115-127.
[34] Lewis R.W., Nithiarasu P., Seetharamu K.N., Fundamentals of the finite element method for heat and fluid flow, John Wiley & Sons, Chichester, 2004.
[35] Arpino F., Carotenuto A., Ciccolella M., Cortellessa G., Massarotti N., Mauro A., Transient natural convection in partially porous vertical annuli, International Journal of Heat and Technology, 34 (2016) S512-S518.
[36] Massarotti N., Ciccolella M., Cortellessa G., Mauro A., New benchmark solutions for transient natural convection in partially porous annuli, International Journal of Numerical Methods for Heat and Fluid Flow, 26 (2016) 1187-1225.
[37] Arpino F., Ciccolella M., Cortellessa G., Massarotti N., Mauro A., Influence of one porous layer insert on the transient heat transfer in a tall annulus in presence of large source terms, International Journal of Heat and Technology, 35 (2017) S478-S484.

ACKNOWLEDGEMENT

The authors express sincere thanks to Dr. Vito Fernicola, Prof. Marco Dell'Isola, Prof. Fausto Arpino, Dr. Giorgio Ficco, Dr. Raffaele D'Alessio and Dr. Fabio Bertiglia for contributing to the realization of the experimental setup.